AGU PUBLICATIONS

JGR

Journal of Geophysical Research: Solid Earth

RESEARCH ARTICLE
10.1002/2015JB012726

Key Points:
- Surface shear wave velocity model onshore and offshore South Island, NZ
- Thin, low-velocity lithosphere beneath inner Campbell Plateau
- Thick, high-velocity lithosphere west of Alpine Fault

Correspondence to:
J. S. Ball,
justin.ball@colorado.edu

Citation:
Ball, J. S., A. F. Sheehan, J. C. Stachnik, F.-C. Lin, W. L. Yeck, and J. A. Collins (2016), Lithospheric shear velocity structure of South Island, New Zealand, from amphibious Rayleigh wave tomography, *J. Geophys. Res. Solid Earth*, *121*, doi:10.1002/2015JB012726.

Received 10 DEC 2015
Accepted 26 APR 2016
Accepted article online 28 APR 2016

Lithospheric shear velocity structure of South Island, New Zealand, from amphibious Rayleigh wave tomography

Justin S. Ball[1], Anne F. Sheehan[1], Joshua C. Stachnik[2], Fan-Chi Lin[3], William L. Yeck[1], and John A. Collins[4]

[1]CIRES and Department of Geological Sciences, University of Colorado Boulder, Boulder, Colorado, USA, [2]Department of Earth and Environmental Sciences, Lehigh University, Bethlehem, Pennsylvania, USA, [3]Department of Geology and Geophysics, University of Utah, Salt Lake City, Utah, USA, [4]Department of Geology and Geophysics, Woods Hole Oceanographic Institution, Woods Hole, Massachusetts, USA

Abstract We present a crust and mantle 3-D shear velocity model extending well offshore of New Zealand's South Island, imaging the lithosphere beneath the South Island as well as the Campbell and Challenger Plateaus. Our model is constructed via linearized inversion of both teleseismic (18–70 s period) and ambient noise-based (8–25 s period) Rayleigh wave dispersion measurements. We augment an array of 4 land-based and 29 ocean bottom instruments deployed off the South Island's east and west coasts in 2009–2010 by the Marine Observations of Anisotropy Near Aotearoa experiment with 28 land-based seismometers from New Zealand's permanent GeoNet array. Major features of our shear wave velocity (V_s) model include a low-velocity ($V_s < 4.4$ km/s) body extending from near surface to greater than 75 km depth beneath the Banks and Otago Peninsulas and high-velocity (V_s~4.7 km/s) mantle anomalies underlying the Southern Alps and off the northwest coast of the South Island. Using the 4.5 km/s contour as a proxy for the lithosphere-asthenosphere boundary, our model suggests that the lithospheric thickness of Challenger Plateau and central South Island is substantially greater than that of the inner Campbell Plateau. The high-velocity anomaly we resolve at subcrustal depths (>50 km) beneath the central South Island exhibits strong spatial correlation with upper mantle earthquake hypocenters beneath the Alpine Fault. The ~400 km long low-velocity zone we image beneath eastern South Island and the inner Bounty Trough underlies Cenozoic volcanics and the locations of mantle-derived helium measurements, consistent with asthenospheric upwelling in the region.

1. Introduction

The South Island of New Zealand sits at the juxtaposition of three different tectonic environments. To the north, the Pacific plate subducts beneath the Australian plate, with a well-defined Benioff zone and abundant deep and intermediate-depth seismicity [*Kohler and Eberhart-Phillips*, 2003]. In Fiordland to the south, the sense of subduction is reversed, with the Australian plate subducting beneath the Pacific plate. Connecting these regions along the west coast of the South Island, the right-lateral Alpine Fault is the surface expression of a continental transform plate boundary.

The islands of present-day New Zealand are the subaerial portion of a much larger submerged continental fragment, Zealandia, which was part of the Gondwana supercontinent until the opening of the Tasman Sea in the Late Cretaceous [*Bache et al.*, 2014; *Cande and Stock*, 2004]. The oldest rocks found in New Zealand are from the Early-Middle Paleozoic Buller (quartz-rich clastics of continental affinity) and Takaka (oceanic arc assemblage) Terranes of the Western Province [*Bradshaw et al.*, 2009; *Cooper and Tulloch*, 1992]. These units are inferred to record complex accretionary processes that occurred along the southeast Gondwana Margin during the Middle-Late Cambrian Ross Orogeny [*Federico et al.*, 2009] and have been correlated with rocks of the Lachlan Fold Belt in eastern Australia [*Bradshaw et al.*, 2009; *Cooper and Tulloch*, 1992]. Rocks of the Western Province are separated from those of the younger Eastern Province by a tectonic boundary, delineated on the surface by the Junction Magnetic Anomaly (JMA) [*Sutherland*, 1999]. Prior to the breakup of Gondwana, Zealandia was likely located seaward of Antarctica and Australia and inboard of the Pacific-Phoenix plate boundary, with the Campbell Plateau contiguous with West Antarctica and the Challenger Plateau separated from the Lachlan Fold Belt by the Lord Howe Rise [*Bache et al.*, 2014]. Convergent conditions mostly dominated the SE Gondwana Margin from the Middle Cambrian through the Early Cretaceous, and seismically imaged northeast

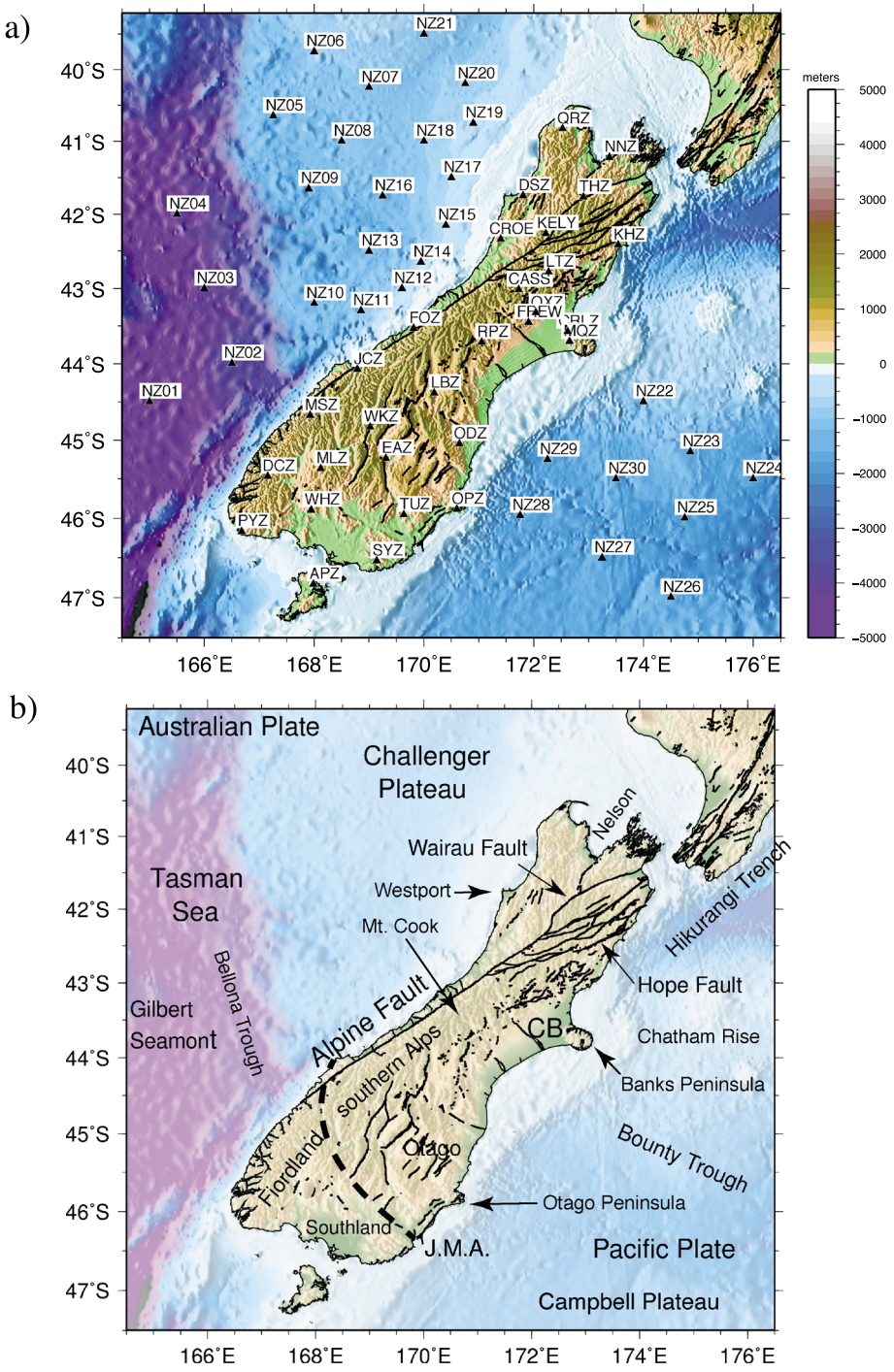

Figure 1. (a) Station map showing location of OBS and land seismic stations. Color scale represents the topography and bathymetry relative to sea level. (b) Regional map showing the main tectonic features. Feature labeled JMA is the trace of the Junction Magnetic Anomaly after *Sutherland* [1999].

dipping crustal/mantle reflectors suggest that relict structures from this long-lived convergent episode are preserved within the Challenger Plateau (Figure 1b) lithosphere today [*Davey*, 2005; *Melhuish et al.*, 2005]. The Hikurangi oceanic plateau subducted beneath the Gondwana Margin at the present-day Chatham Rise, approximately 105–96 Ma before plate motion was reconfigured and the stalled subducted slab south of Chatham Rise is hypothesized to have detached and sunk [*Davy et al.*, 2008; *Hoernle et al.*, 2006]. The breakup of Gondwana

initiated with widespread continental rifting and extension beginning ~100 Ma, whereafter Zealandia transitioned to a passive margin setting when Tasman Sea spreading began approximately 85 Ma [*Bache et al*., 2014]. The opening of the Tasman Sea ceased around 52 Ma when the Lord Howe Rise and Australian plates joined [*Cande and Stock*, 2004]. Plate reconstructions indicate that the Zealandian Australia/Pacific plate boundary likely initiated at this time, cutting across the Challenger Plateau [*Cande and Stock*, 2004], possibly in the location of the present-day Alpine Fault [*Sutherland et al*., 2000]. Eocene rifting along the Resolution Ridge (Figure 1b) beginning approximately 45 Ma likely created oceanic crust eastward of the present-day Alpine Fault, which is no longer present in surface rocks and is inferred to have been overridden by the Campbell Plateau (Figure 1b) during Cenozoic convergence [*Spasojević and Clayton*, 2008; *Sutherland et al*., 2000]. The Eocene rifting episode requires a pair of passive margins, one of which is evidently preserved at the western edge of the Campbell Plateau. Plate reconstructions suggest that the conjugate margin, and possibly the missing Eocene oceanic lithosphere, have been incorporated into the continental collision zone beneath the Alpine Fault since the Miocene [*Sutherland et al*., 2000]. The present-day Alpine Fault initiated with slow, diffuse transtension around 45 Ma, which evolved into almost purely strike-slip motion by 25 Ma [*Sutherland et al*., 2000].

Sutherland et al. [2000] propose that the evolution and morphology of the present-day plate boundary could be controlled by lithospheric discontinuities extant since the Paleozoic and manifested in the location of the Eocene passive margin, while *Reyners* [2013] proposes that the continental collision process since the Cenozoic has been influenced by the ongoing subduction of the Hikurangi oceanic plateau (Figure 1b). The continuous elastic response of the lithosphere to shortening imposed between the oppositely verging subduction zones of Hikurangi and Fiordland was numerically modeled by *Pysklywec et al*. [2010], with resulting models showing along-strike variations in the morphology of the lithospheric root.

Much of the continental lithosphere of Zealandia is below sea level and not easily accessible for seismic studies to probe the nature of the plate boundary and adjacent mantle lithosphere. Previous work using New Zealand land-based seismic stations has produced images of crustal structure from ambient noise surface wave tomography [*Lin et al*., 2007], Moho depth from receiver functions [*Spasojević and Clayton*, 2008], and body wave tomography for crust and mantle structure [*Kohler and Eberhart-Phillips*, 2002]. Teleseismic shear wave splitting analysis [*Zietlow et al*., 2014] and Pn travel time residuals [*Collins and Molnar*, 2014] reveal a pattern of lithospheric anisotropy consistent with strain distributed across an ~200 km region parallel to the Alpine Fault, but uncertainty persists as to the depth extent of localized versus distributed shear as revealed by seismic anisotropy. The latter two studies utilized an array of 29 broadband ocean bottom seismometers (OBSs) deployed from 2009 to 2010 in the Marine Observations of ANisotriopy off Aoteroa (MOANA) experiment [*Yang et al*., 2012], with the primary objective of using these anisotropy measurements to characterize the distribution of strain about the plate boundary.

In this study we utilize ocean bottom seismometers offshore both east and west coasts of the South Island of New Zealand, and along with existing land-based seismometers, perform surface wave tomography for Rayleigh wave group and phase velocities using ambient noise and earthquake data recorded at periods from 8 to 70 s. The incorporation of ocean bottom seismometers greatly increases the array aperture available to interrogate both the onshore and offshore portions of the New Zealand continental lithosphere, resulting in improved resolution for the land portion of the study area, and the first lithospheric shear velocity models of offshore Campbell and Challenger Plateaus.

2. Data and Methods

Ambient noise and teleseismic surface wave analysis is conducted using waveforms collected by the 29 MOANA OBS stations and 28 land-based stations, 24 of which are from the permanent New Zealand GeoNet network [*Petersen et al*., 2011] shown in Figure 1. The OBS stations were deployed between February 2009 and February 2010 over an ~900 × 1300 km area centered on South Island. The average station spacing was ~100 km. The OBS instrument packages included three-component seismometers with 240 s lower corner frequencies (excepting one 40 s sensor) and Cox-Webb differential pressure gauges (DPGs) with long-period sensitivity extending to over 1000 s [*Webb and Crawford*, 1999]. Data were digitized continuously at a sample frequency of 50 Hz. Seismic data quality on the OBS vertical component can approach or exceed that of quiet land stations in the "noise notch" [*Webb and Crawford*, 1999] at periods between ~10 and 40 s. MOANA OBS station performance is described in more detail in *Yang et al*. [2012].

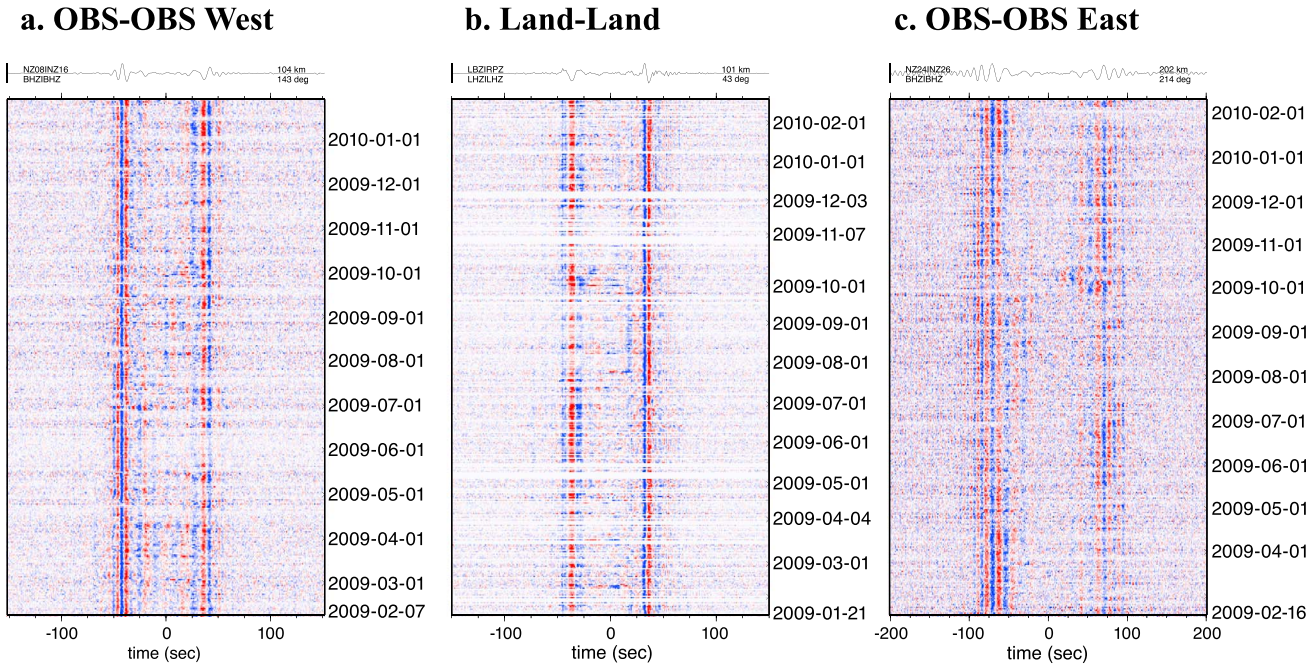

Figure 2. Yearly stacks (waveforms at top) of 24 h ambient noise Green's functions used in this analysis. Cross correlations between selected OBS stations in the (a) Tasman Sea, (b) land stations, and (c) OBS in the Bounty Trough are shown.

2.1. Ambient Noise Cross Correlation

Interstation group and phase velocity dispersion measurements are obtained from ambient noise cross correlations calculated between all station pairs for every hour of data between February 2009 and February 2010 using the method of *Stachnik et al*. [2008]. We downsample the continuous vertical component seismic waveforms from 50 samples per second (sps) to 1 sps and preprocess by removing the linear trend and instrument responses before band-pass filtering from 3 to 100 s to mitigate artifacts during cross correlation. The waveforms are then Fourier transformed, the amplitude spectrum is prewhitened, and the cross correlation is performed in the frequency domain. This method is similar to time domain 1 bit normalization techniques in its effectiveness at suppressing transient signal contamination [*Bensen et al*., 2007]. Information about absolute amplitudes is lost with both of these methods; however, it is not needed to calculate interstation group and phase velocity, and the amplitude-normalizing techniques allow data to be utilized and stacked in the absence of source information.

The hourly cross correlations for a given station pair are stacked to give a day record and archived in a database. All available day records for each station pair are then stacked to yield an experiment average cross-correlation function for each station pair. Examples of stacked interstation cross correlations are shown in Figure 2 for different combinations of OBS stations and land-based stations. Clear Rayleigh wave packets are visible with propagation speeds expected of surface waves. Cross correlations for ocean-ocean and ocean-land paths all show clear and symmetric Rayleigh wave packets for both the causal and acausal signal implying good azimuthal distribution of ambient noise sources (Figure 2). Rayleigh waves are consistent over the duration of the experiment, which encompassed both austral summer and winter cycles, indicating minimal temporal seasonal bias. Cross correlations between OBS stations on opposite sides of the island and those between land and OBS stations are less symmetric yet still reveal good signal-to-noise ratio (SNR) and dispersive characteristics.

Fundamental mode Rayleigh wave dispersion is measured for each station pair from the stacked cross correlation using frequency-time analysis [*Dziewonski and Hales*, 1972]. Similar to *Lin et al*. [2008], the amplitudes of the positive and negative lag times of the cross correlations are averaged to extract a Rayleigh wave packet unbiased by signal strength related to direction of propagation and source distribution.

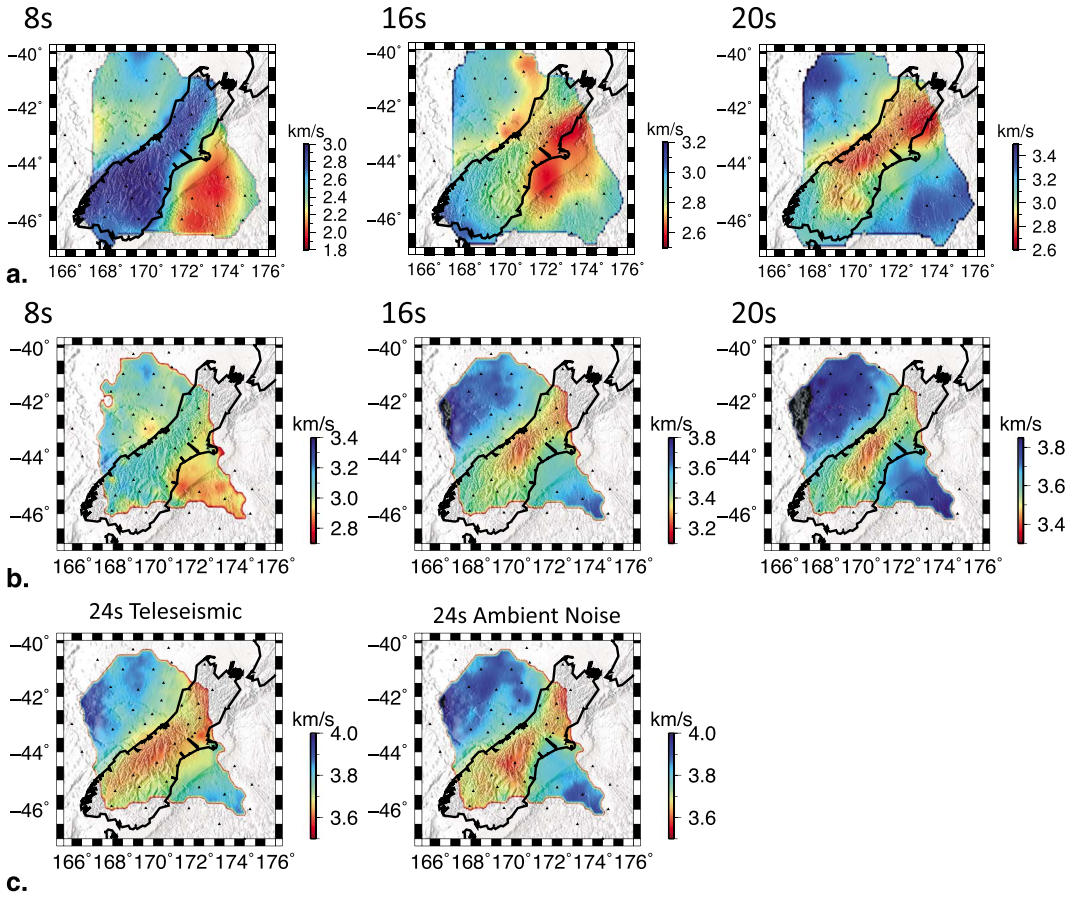

Figure 3. (a) Isotropic group velocity maps derived from ambient noise tomography at periods of 8–25 s. (b) Phase velocity maps derived from ambient noise tomography at periods of 8–24 s. (c) Phase velocity maps derived from (left) teleseismic data and (right) ambient noise tomography at 24 s period.

The period band of reliable dispersion measurements is determined by calculating signal-to-noise ratio of the Rayleigh wave envelope relative to the root-mean-square of cross-correlation amplitudes more than 50 s past the timing of an arrival with velocity 2.0 km/s. We measure group and phase velocity dispersion at periods from 8 to 25 s from the interstation Green's functions using the frequency-time analysis (FTAN) method of *Levshin et al.* [1972]. We employ the automated FTAN software aftan 1.1 (http://ciei.colorado.edu/Products/, last accessed 19 May 2014). The group velocity is determined by applying a sequence of narrowband Gaussian filters to the cross correlation and selecting the peak of the envelope within a reasonable group velocity window (1.4–4.5 km/s). The dispersion curves are the mean group velocity calculated at periods from 8 to 25 s after culling based on group velocity standard deviation less than 0.10 km/s and SNR greater than 10. Subsequently, we remove all measurements exceeding 3 standard deviations from the mean, and those where interstation distance is less than two wavelengths, calculated given the velocity and period. We use the two-wavelength criterion following *Lin et al.* [2013] and *Yao et al.* [2011] to preserve more measurements at long periods, given the relatively short interstation distances in the MOANA array. Cumulatively, these culling steps remove ~20% of our measurements.

2.2. Ambient Noise Group Velocity Tomography

To transform the culled path-dependent interstation dispersion measurements into a set of period-dependent 2-D group velocity maps we employ the straight-ray tomographic inversion method of *Barmin et al.* [2001]. We use the software package tomo_sp_cu_s 1.1 (http://ciei.colorado.edu/Products, last accessed 19 May 2014). This software performs a damped least squares inversion, producing isotropic and anisotropic 2-D group and phase velocity maps at periods from 6 to 30 s. While we analyze only the resulting isotropic

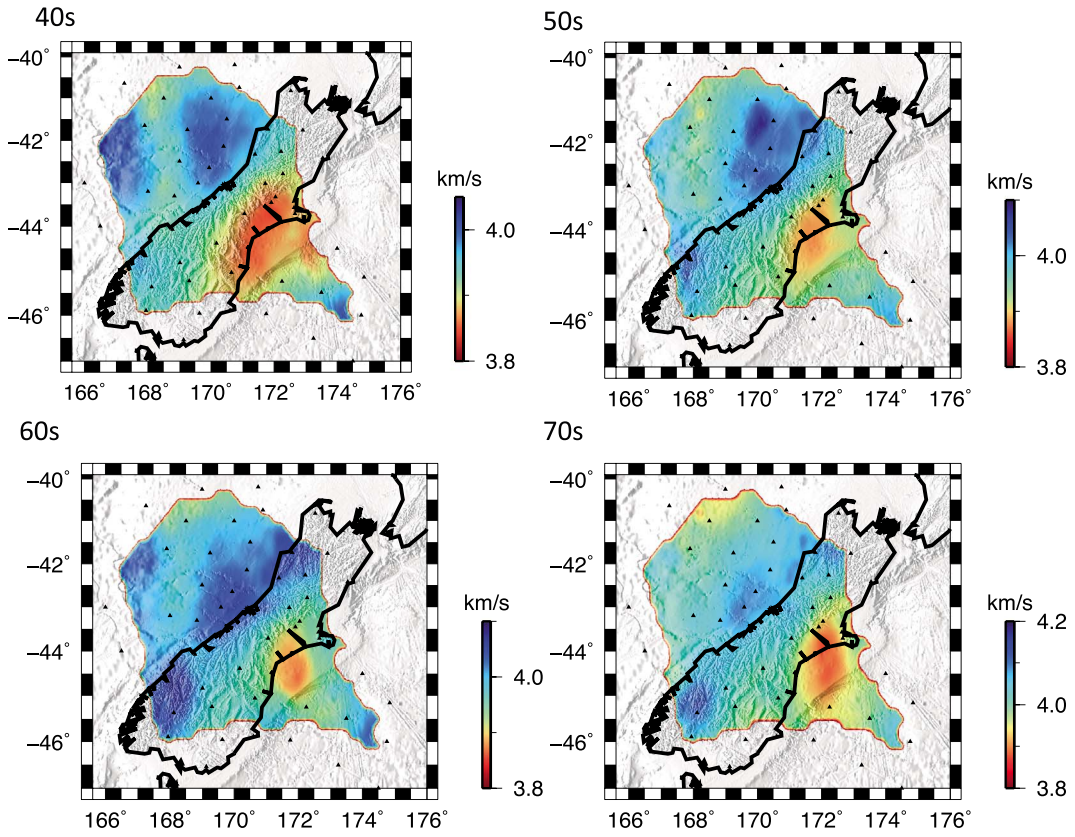

Figure 4. Phase velocity maps from teleseismic tomography at periods of 40–70 s.

group and phase velocity maps here (Figures 3 and 4), the anisotropic group velocity maps are interpreted in *Yeck* [2015]. We also generate maps of azimuthal coverage, ray density, and resolution (Figure 5). The spatial resolution maps (Figure 5) are a measure of the minimum distance from each node at which a delta-shaped anomaly can be distinguished by the tomographic inversion from an identical delta function at the target node. In accordance with prior applications of this tomographic method [*Lin et al.*, 2008], resolution is finest in the center of the array (where the largest number of interstation paths cross) and decreases in quality toward the edges of the array. The tomography produces Cartesian maps with a node spacing of 0.5°, which we then interpolate to resample the maps at 0.2° node spacing. The resulting group speed maps are shown in Figure 3.

2.3. Ambient Noise and Teleseismic Phase Velocity Tomography

At a given period, Rayleigh wave phase velocity dispersion generally depends on deeper velocity structure than group dispersion [*Yao et al.*, 2011]. The addition of teleseismic (earthquake) dispersion measurements enables longer periods, and thus deeper lithospheric shear velocities, to be modeled [*Gaite et al.*, 2015] compared with noise-based measurements alone. Therefore, to complement our group velocity measurements from straight-ray tomography and resolve deeper structure, we also measure phase velocities from both noise cross-correlation functions (8–24 s period) and teleseismic Rayleigh wave signals (18–70 s period). All available vertical component waveforms for earthquakes with $M_s > 5.0$ are analyzed. High noise levels are commonly observed at shallow OBS stations at long periods (>30 s), which necessitates special treatment before these data can be further analyzed. This long-period noise is clearly correlated with pressure perturbations observed by the co-located differential pressure gauges (DPGs) and is likely caused by seafloor compliance or the deformation of the seafloor under loading by ocean surface infragravity waves. Seafloor compliance is defined by the transfer function between displacement and pressure at the seafloor [*Crawford and Webb*, 2000] and is sensitive to sediment rigidity and thickness [*Ball et al.*, 2014]. To reduce the compliance noise level, we implement the method described by *Crawford and Webb* [2000]. For a quiet day (9 June 2009) with no detectable earthquakes in the observed waveforms, we calculate the transfer

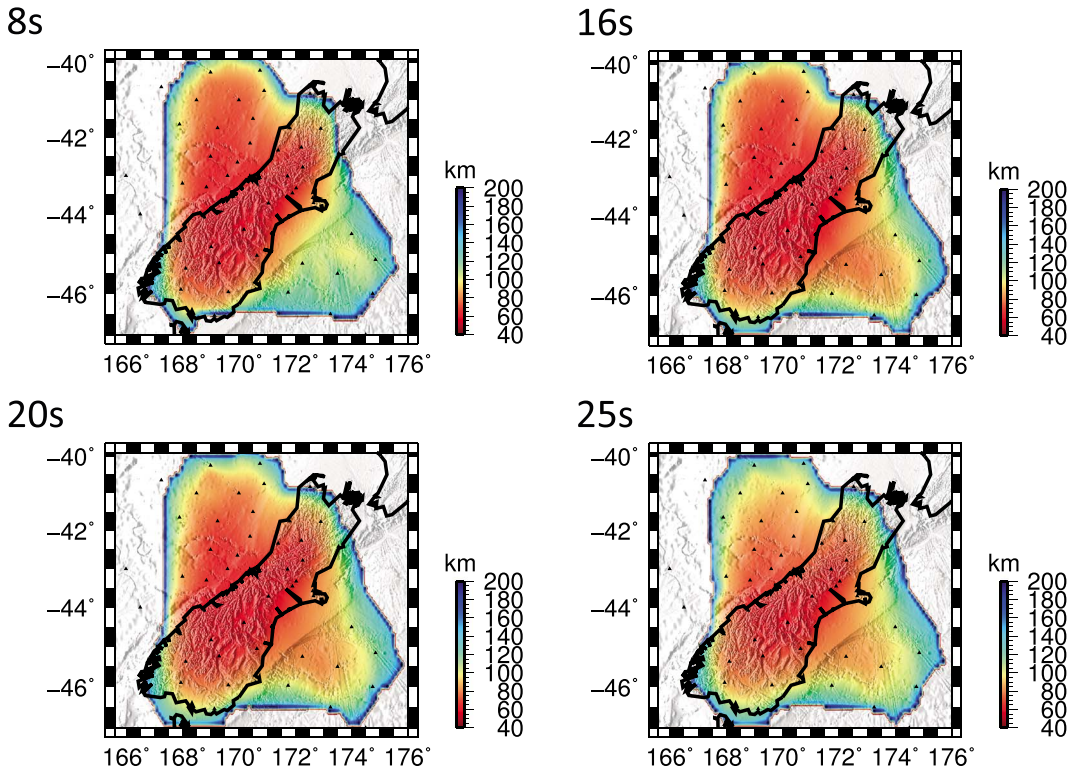

Figure 5. Resolution maps from straight-ray ambient noise group velocity tomography procedure at periods from 8 to 25 s.

function between the vertical component OBS and DPG measurements for each station. The transfer function is then used to predict and remove the compliance signal in the vertical component due to pressure perturbation for any other days.

We follow closely the eikonal tomography method described by *Lin et al*. [2009] to determine Rayleigh wave phase velocity maps across the array for the noise correlation functions and teleseismic data. For each station and earthquake, and each interstation noise correlation function, we first perform frequency-time analysis (FTAN) [*Levshin et al*., 1972] to obtain dispersive phase travel time measurements. For each earthquake and period, all measurements with SNR higher than 8 are then used to determine the phase travel time map. Note that we follow the phase front tracking method described by *Lin and Ritzwoller* [2011] to resolve the 2π ambiguity in phase velocity measurements and we determine the travel time maps on a 0.2°×0.2° grid through the minimum curvature surface fitting [*Smith and Wessel*, 1990]. Based on the eikonal equation, we estimate the phase velocity at each location using the gradient of each phase travel time map. For each period, all phase velocity measurements at the same location are averaged to obtain the final isotropic phase speed maps for both noise and teleseismic data. The resulting noise-based and teleseismic phase speed maps are shown in Figures 3 and 4. A comparison of noise and teleseismic phase speed measurements at a common period (24 s) is shown in Figure 3c. While the noise and teleseismic data set data generally agree well, subtle differences are apparent, likely resulting from an inhomogeneous noise source distribution and/or differing finite-frequency sensitivities between data sets [*Yao and van der Hilst*, 2009]. Period-dependent measurement uncertainties are estimated following *Lin et al*. [2009], and uncertainty maps are shown in Figure 6. For both noise-based and teleseismic data sets, measurement uncertainty is lowest in the center of the analyzed period ranges (Figure 6).

2.4. Inversion for 1-D Shear Velocity Profiles

We sample the Rayleigh wave group and phase velocity tomograms at 0.2° increments in latitude and longitude to determine local dispersion curves at each node. At each node, the local group and phase dispersion curves are simultaneously inverted for a one-dimensional isotropic shear velocity (V_s) profile using depth

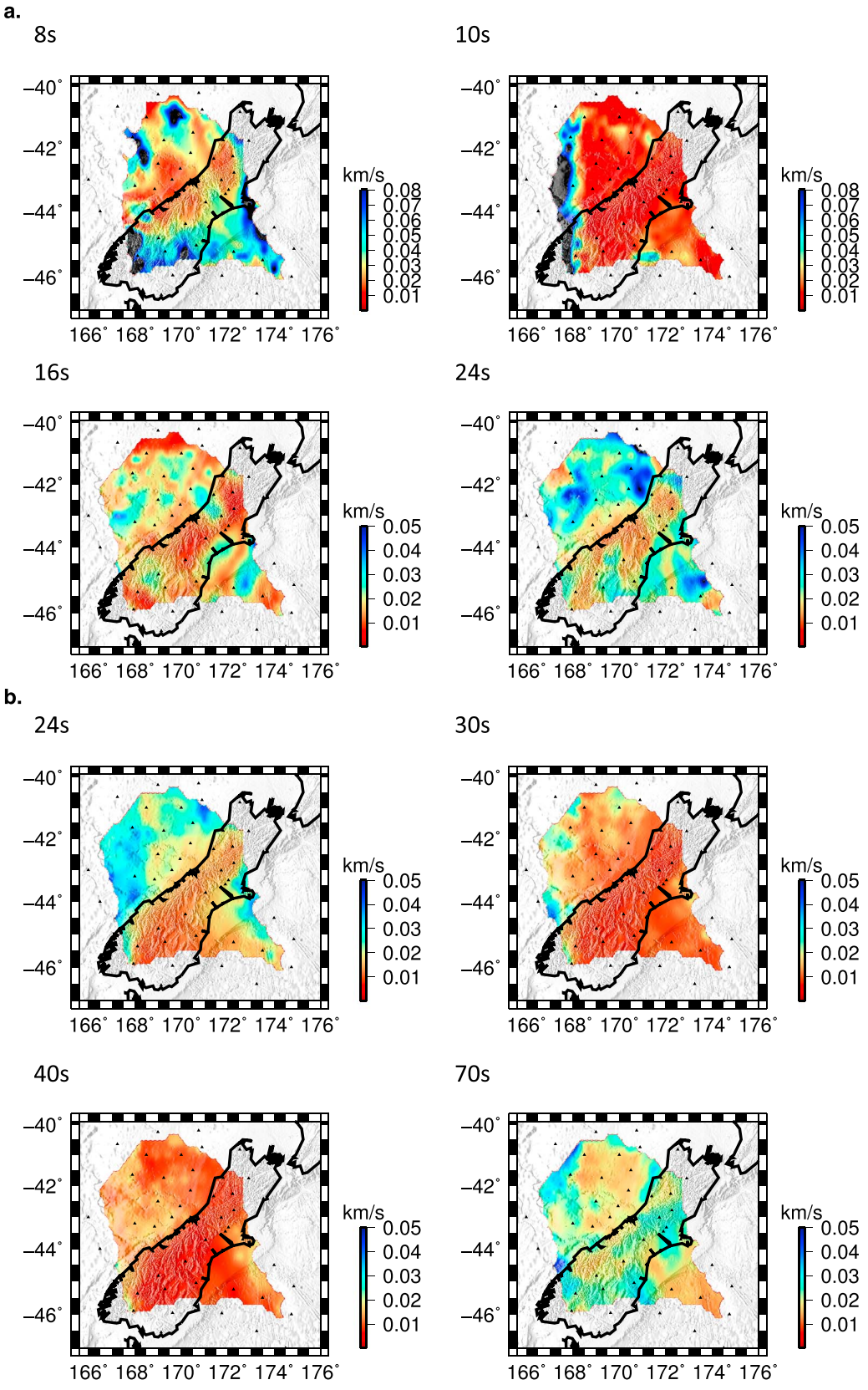

Figure 6. (a) RMS uncertainty maps for ambient noise-derived phase velocity measurements at periods from 8 to 24 s. (b) Maps of RMS uncertainty of teleseismic phase velocity measurements at periods from 24 to 70 s.

sensitivity kernels and the linearized least squares method of *Herrmann and Ammon* [2004]. The software performs an iterative, damped inversion, computing-updated sensitivity kernels at each iteration to minimize the dependence on the starting model. We fix the V_p/V_s ratio in the medium to that of the initial model and iteratively invert for the V_s of each layer. Density is calculated from the new V_p at each iteration using the Nafe-Drake equation [*Nafe and Drake*, 1957].

The inversion minimizes an objective function of the form [*Aster et al*., 2013, *Hosseini*, 2014]:

$$F = \|\mathbf{J}(\mathbf{m})(\mathbf{m}+\Delta\mathbf{m}) - (\mathbf{d} - \mathbf{G}(\mathbf{m}) + \mathbf{J}(\mathbf{m})\mathbf{m})\|_2^2 + \lambda^2\|\mathbf{L}(\mathbf{m}+\Delta\mathbf{m})\|_2^2 \quad (1)$$

where **m** is a vector of unknown model parameters (i.e., shear velocities in each layer) perturbed by $\Delta\mathbf{m}$, **d** is the observed data vector (group and phase velocities), and **J**(**m**) is the Jacobian matrix containing partial derivatives of the forward equation **G**(**m**) with respect to the model parameters (in this case **J**(**m**) contains partial derivatives of group and phase velocity with respect to shear velocity in each layer). The finite difference operator $\mathbf{L}(\mathbf{m}+\Delta\mathbf{m})$ includes a matrix of weights controlling model smoothness by limiting the change in velocity across each layer [*Herrmann and Ammon*, 2004], and λ is the damping (regularization) parameter.

We use a high damping parameter (10) in the first iteration to mitigate model overshoot effects and lower the damping to 0.3 for subsequent iterations. We chose the damping parameter and number of iterations (10) via trial and error to optimize the trade-off between model roughness and data misfit. We apply moderate weighting (0.8) to the layers in the uppermost 20 km to smooth the upper crustal model. Below 20 km individual layer weighting is decreased with depth, so that the deepest layers from 180 to 600 km (exceeding the peak depth sensitivity of our dispersion data) remain unperturbed from the reference model. The starting model for the V_s inversion is based on the ak135 reference Earth model of *Kennett et al*. [1995]. The velocities of the uppermost 50 km of the starting model are constant, set to the 43 km depth ak135 values of $V_p = 8.04$ km/s and $V_s = 4.48$ km/s, in order to eliminate bias from the ak135 model's Moho depth. Below 50 km the starting model follows ak135 velocities with depth. We parameterize the model space using 2 km thick layers in the upper 50 km, increasing to 5 km thick layers down to 100 km. Below 100 km, layers are 10 km thick. The increasing layer thicknesses with depth were chosen by trial and error to optimally match the depth sensitivity of our dispersion data. In offshore regions the local starting model is capped by a layer of zero shear velocity with thickness equal to the water depth taken from the SRTM30_PLUS global elevation and bathymetry model [*Becker et al*., 2009]. The velocity and thickness of this water layer are fixed during the iterated linearized inversion.

We perform the inversion twice, once with no a priori crustal thickness estimates and once incorporating estimates of Moho depth from *Salmon et al*. [2013]. In the constrained Moho inversion we identify the model layer corresponding to the estimated Moho depth and force a velocity contrast to exist across that layer by increasing the layer's weight by a factor of 5. The crustal thickness model of *Salmon et al*. [2013] incorporates results from onshore/offshore refraction and reflection studies dating to the 1980s and includes Moho depth estimates from recent onshore receiver function analyses [*Spasojević and Clayton*, 2008]. Where data are sparse (i.e., offshore), they are interpolated using the Crust2.0 model [*Bassin et al*., 2000]. This model is well constrained by dense data sets in some areas (onshore and offshore areas with active source lines) and poorly constrained in others (offshore away from active source lines). Representative 1-D velocity models with and without Moho constraint are shown in Figure 7. In the models shown, imposing the Moho constraint tends to reduce both data misfit at longer periods and the relative variance of deeper velocities between nodes.

3. Shear Velocity Inversion Results

Major features of our 3-D shear velocity model that we interpret here (Figures 8–10) include a southward dipping high-speed ($V_s > 4.5$ km/s) body underlying the South Island south of Mount Cook (labeled as anomaly passive margin (PM) in Figure 10), a lower-velocity ($V_s < 4.4$ km/s) body underlying the Canterbury/Otago region and Bounty Trough (anomaly asthenospheric upwelling (AU) in Figure 10a), and a deep (>100 km) high-velocity ($V_s > 4.5$ km/s) zone extending offshore the northwestern coast of the South Island beneath Challenger Plateau (anomaly CP in Figure 10a). Depth slices at 15–140 km are shown in Figure 8. Figure 9 shows V_s model cross sections perpendicular to the strike of the Alpine Fault and extending from the

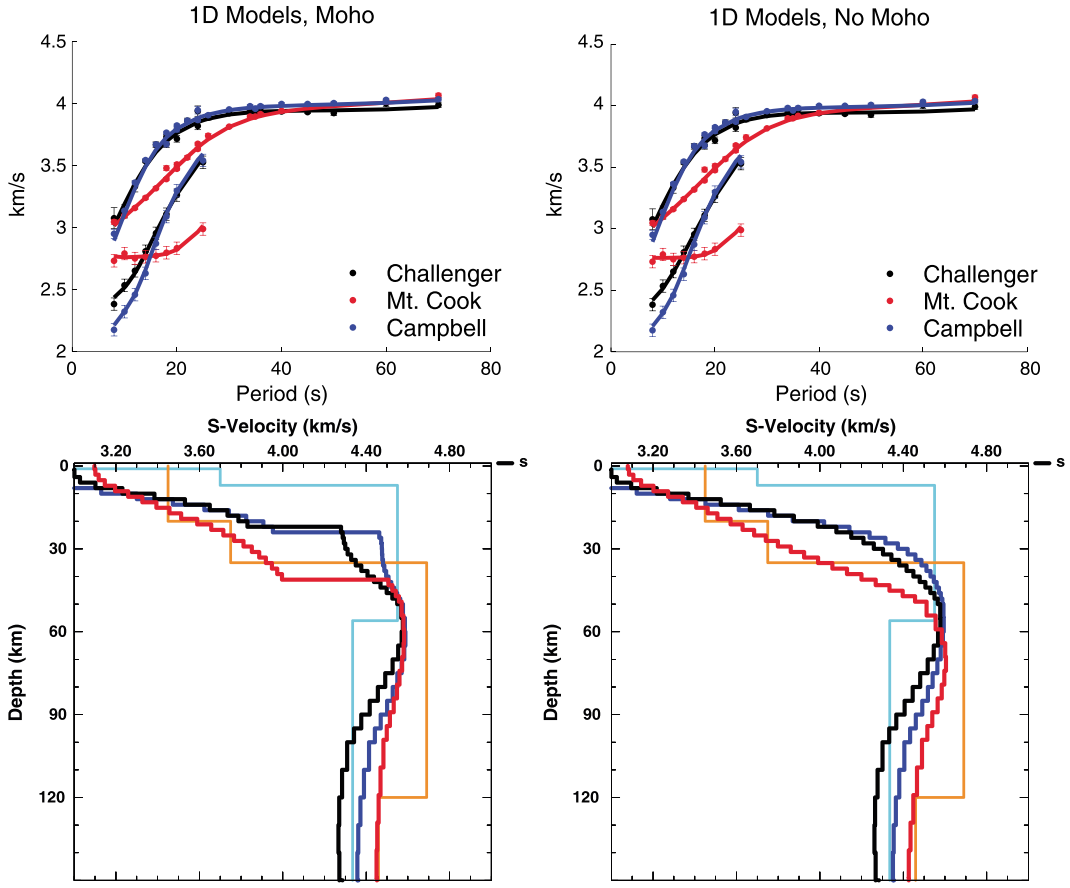

Figure 7. (top) Data fits and (bottom) 1-D models resulting from inversions (left column) with and (right column) without Moho constraint from *Salmon et al.* [2013]. Blue and orange lines show the PEM-O and PEM-C reference Earth models, respectively, from *Dziewonski et al.* [1975].

Tasman Sea across the South Island to the Bounty Trough and fault-parallel transects spanning the central South Island and the Challenger and Campbell Plateaus.

At shallow depth (15 km) in our model, the most prominent feature we resolve is an arcuate lateral velocity discontinuity cutting across the southern South Island (Figure 8a), which generally follows the trace of the Junction Magnetic Anomaly (Figure 1). To the north of this zone, crustal shear velocities are ~3.4 km/s at 15 km depth, while to the south they exceed 3.6 km/s. At a depth of 40 km (Figure 8c) we observe an apparent crustal root with shear velocities less than 3.8 km/s underlying the Southern Alps, in contrast with surrounding higher shear velocities ($>$4 km/s) characteristic of upper mantle material. The imposition of a Moho constraint focuses this crustal root beneath the highest topography of the Southern Alps in the 40 km depth slice (Figure 8c).

The central South Island upper mantle high-velocity anomaly in our model at depths below 50 km (anomaly PM in Figure 10) dips southward from Mount Cook beneath the Southern Alps (Figures 9b, 9e, and 10). The depth of highest shear velocities beneath central South Island ranges from ~80 km beneath Mount Cook to over 100 km beneath Fiordland.

The northern, offshore Challenger Plateau high-velocity anomaly we image (anomaly CP in Figure 10a) extends several hundred kilometers northwestward from the west coast, with the highest shear speeds concentrated at depths below 80 km and latitudes below 43°S (Figures 8e–8h). We also resolve a low-velocity zone (anomaly AU in Figure 10a) at depths from 60 to 150 km beneath the east coast of South Island which underlies the Otago Peninsula at the shallowest depths (Figure 8d) and, with increasing depth, increases in lateral extent beneath the Canterbury Basin (Figures 8e–8h), underlying the entire inner Bounty Trough at 150 km depth.

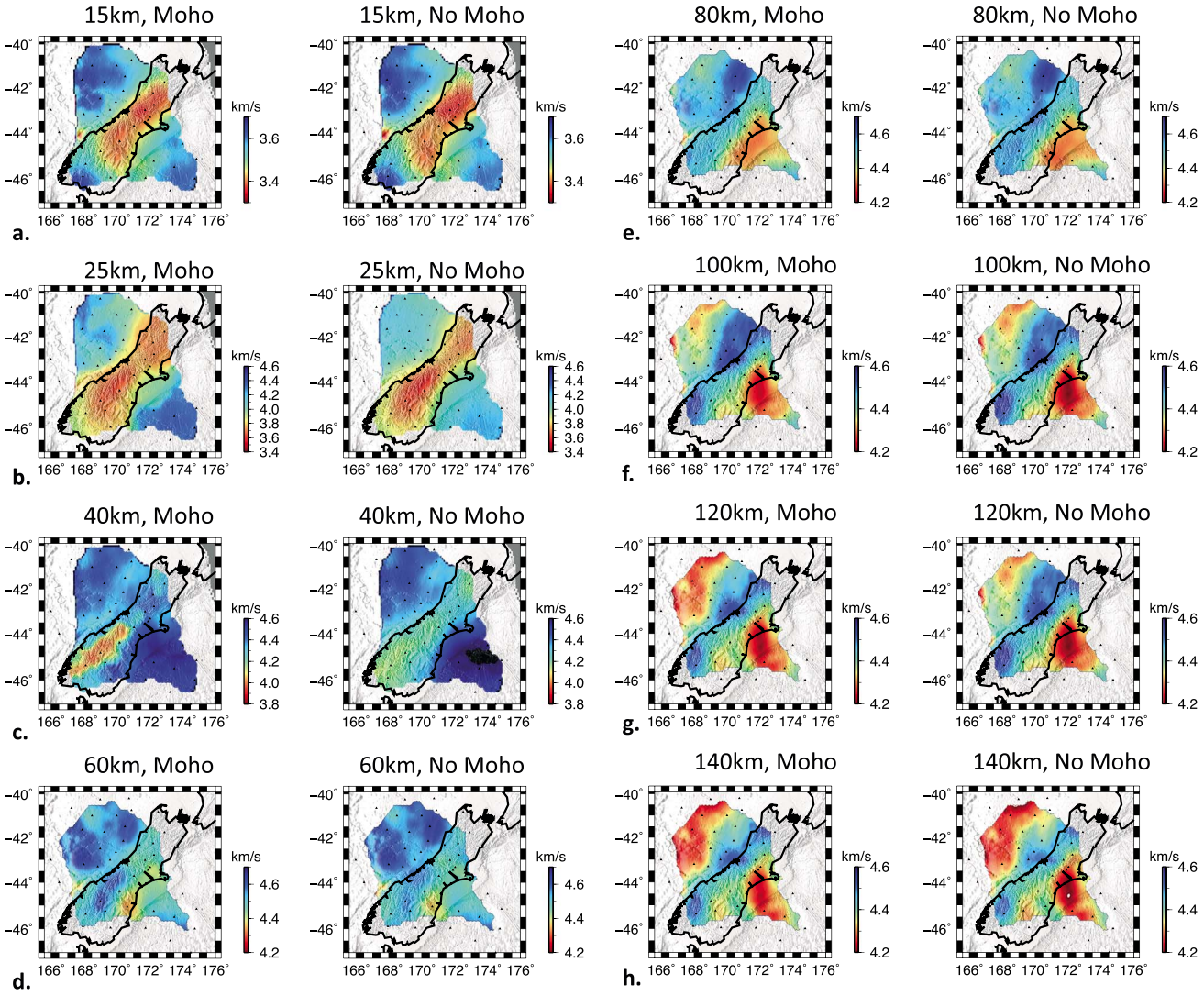

Figure 8. Depth slices through final shear velocity model, from $z = 15$ km to $z = 140$ km. (left column) Maps result from inversion using Moho depth constraint from *Salmon et al*. [2013]. (right column) Maps result from unconstrained inversion.

4. Discussion

4.1. Challenger Plateau

We image a zone of high shear velocities ($V_s > 4.6$ km/s) offshore the northwestern coast of South Island and extending southward along the west coast (Figures 8e–8h), with the highest shear speeds extending in depth from 50 to 150 km beneath the Challenger Plateau. This anomaly is labeled CP in Figure 10a. In the northernmost part of the South Island an apparent continuation of this feature is resolved to greater depths (>300 km) with teleseismic body wave tomography by D. W. Zietlow et al. (Teleseismic *P* wave tomography of South Island, New Zealand upper mantle: Evidence of subduction of Pacific lithosphere since 45 Ma, submitted to *Journal of Geophysical Research*, 2016), who interpret it as subducted Pacific plate lithosphere. While observed Benioff zone seismicity associated with modern Hikurangi subduction [*Reyners*, 2013] does not extend nearly as far westward of the Alpine Fault as the high-velocity feature we model at depth, we too consider westward subducted lithosphere to be the simplest explanation for anomaly CP.

The continental lithosphere of the Challenger Plateau off the west coast of the South Island is at least Paleozoic in age [*Sutherland et al*., 2000], and dipping mantle reflectors that have been interpreted as relict structures from Gondwana Margin subduction [*Davey et al*., 2005; *Fry et al*., 2014; *Melhuish et al*., 2005]

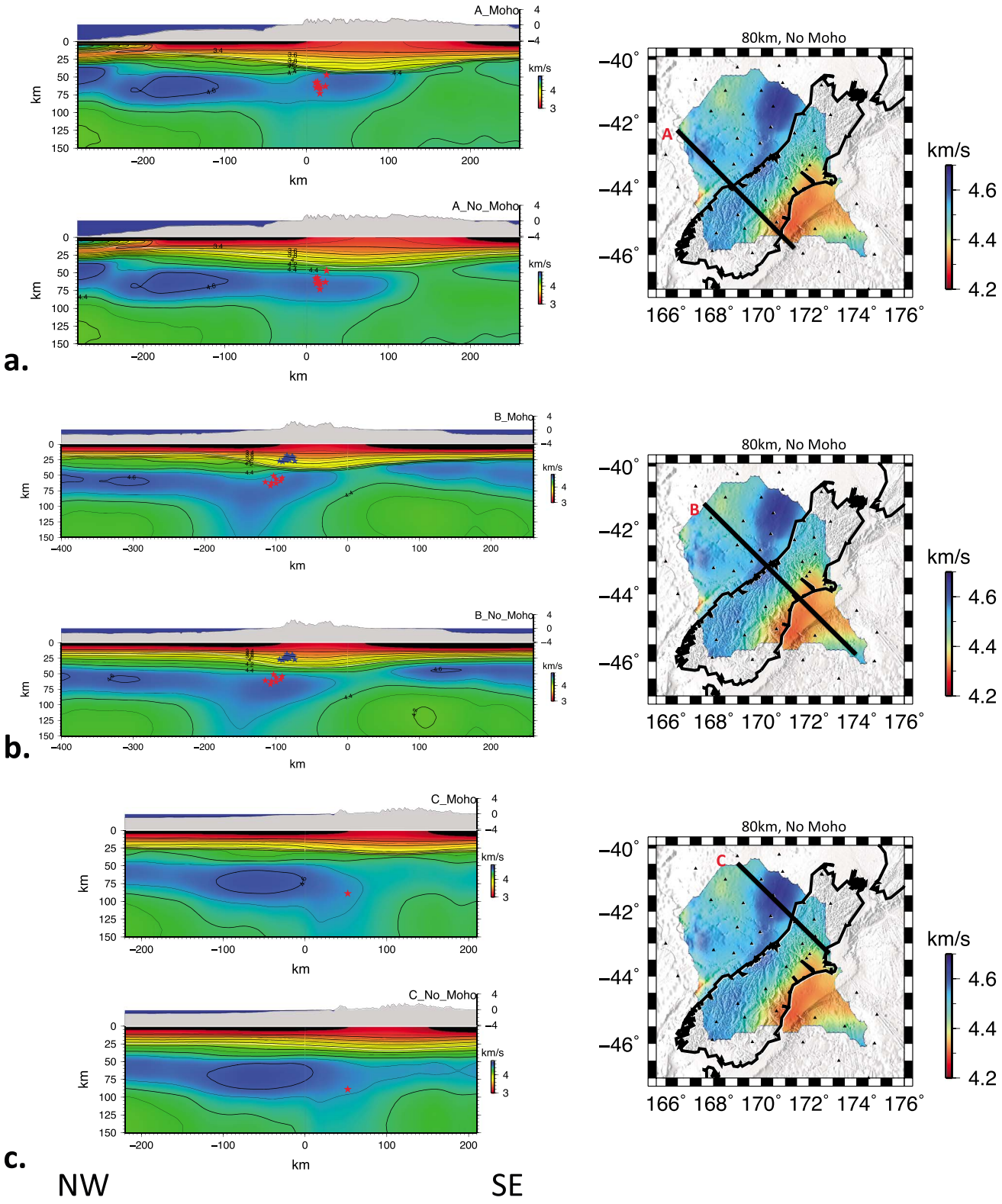

Figure 9. Cross sections through final V_S models. (top) Cross section in each subplot shows model resulting from inversion with Moho depth constraint of *Salmon et al*. [2013] and (bottom section) shows unconstrained inversion result. (right column) Transect locations are shown on maps, overlain on the 80 km unconstrained depth slice shown in Figure 8e. Red stars on sections a, b, c, and e are the subcrustal earthquake hypocenters presented in *Boese et al*. [2013]. Blue stars are the low-frequency earthquake (LFE) hypocenters reported by *Chamberlain et al*. [2014].

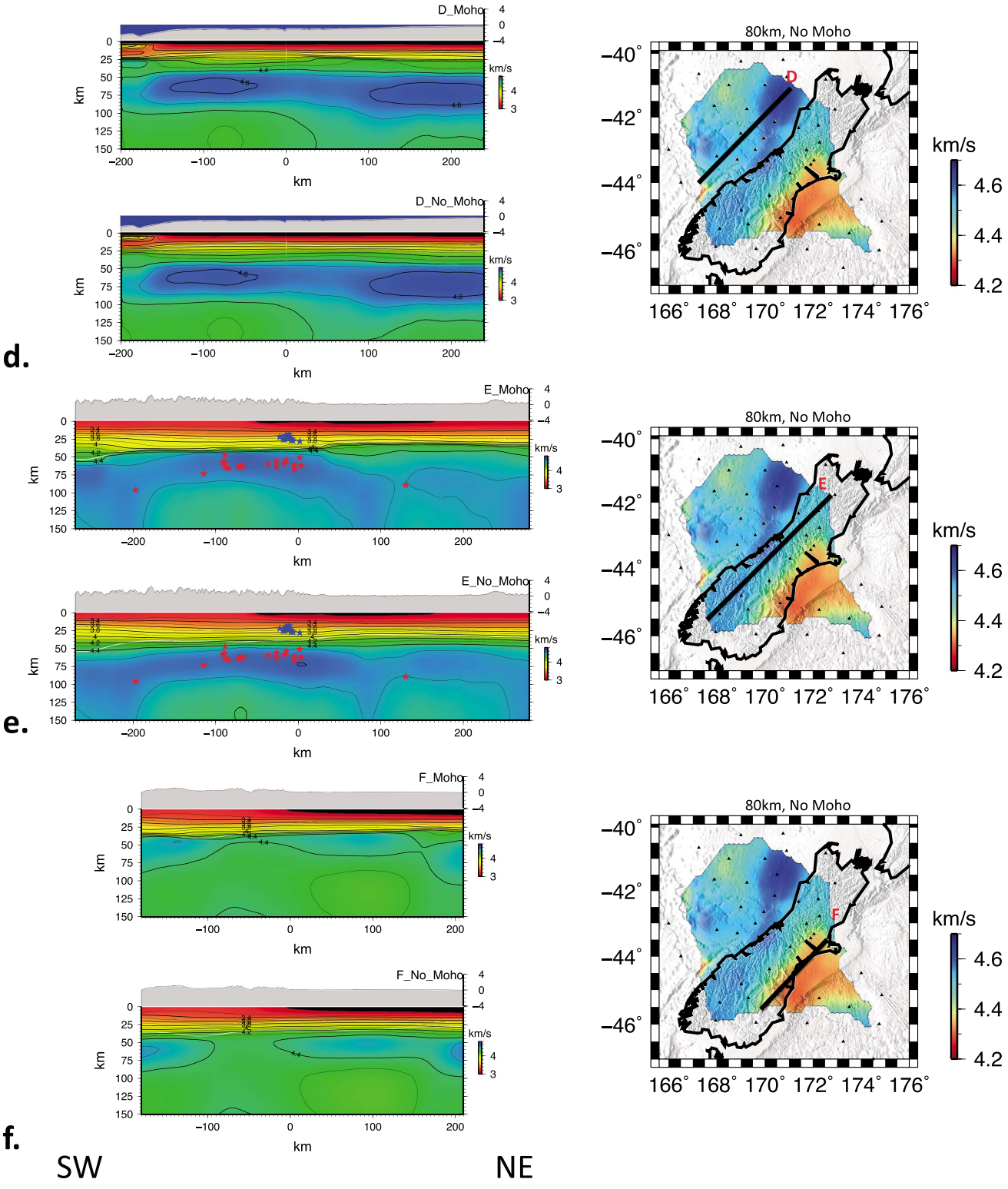

Figure 9. (continued)

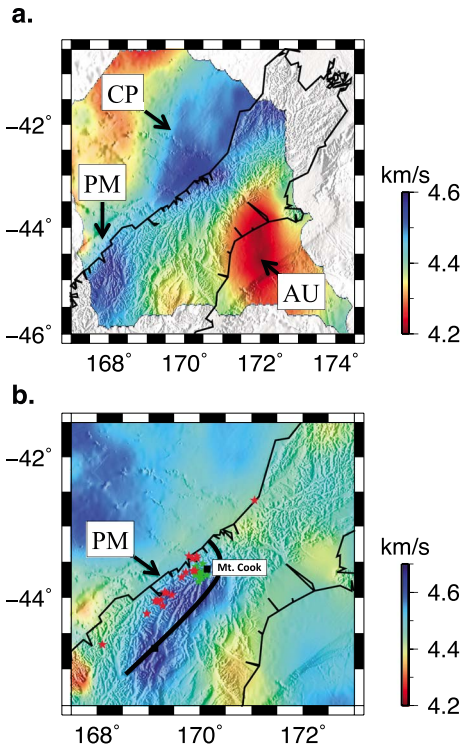

Figure 10. (a) Anomalies interpreted in section 4 are labeled on a 100 km depth slice of our Moho-constrained model. Anomaly CP (Challenger Plateau) is discussed in sections 4.1 and 4.4 and interpreted as thickened Australian/Pacific lithosphere and/or subducted Pacific lithosphere. Anomaly PM (passive margin) is discussed in section 4.2 and shown in more detail in Figure 10b. Anomaly AU (asthenospheric upwelling) is discussed in sections 4.3 and 4.4 and interpreted to as upwelling asthenosphere/detached lithosphere. (b) The 50 km Moho-constrained model depth slice. Anomaly PM (passive margin) is discussed in section 4.2 and coincides with the hypothesized location of a relict Eocene passive margin overridden by the South Island [*Sutherland et al.*, 2000]. Red stars are the subcrustal hypocenters [*Boese et al.*, 2013], green stars are the tremor locations [*Chamberlain et al.*, 2014], and black line is the inferred leading edge of the passive margin from *Boese et al.* [2013].

coincide with the southwest boundary of the Challenger Plateau high-velocity anomaly we image (anomaly CP in Figure 10a).

Both group velocity resolution scale (Figure 5) and phase velocity RMS uncertainty (Figure 6) generally increase toward the outer stations of the array. Thus, uncertainty in the velocity structure we image beneath Challenger Plateau increases with increasing distance from South Island, tempering our interpretation.

4.2. Onshore South Island

Our results onshore South Island generally agree with the onshore velocity models presented by *Fry et al.* [2014] and *Lin et al.* [2007]. In the crust we observe a change in shallow velocity structure that correlates spatially with the Junction Magnetic Anomaly (JMA) [*Sutherland*, 1999] across southern South Island (Figures 1b, 8a, and 8b) at 15 km depth. We find that crustal shear velocities north of the JMA are systematically slower than those south of the JMA by roughly 10%.

The mantle high-velocity zone extending southward of Mount Cook that we denote as anomaly PM (Figure 10) is spatially correlated with reverse and strike-slip mantle earthquakes presented by *Boese et al.* [2013] and appears to align with the location of an inferred relict Eocene passive margin [*Sutherland et al.*, 2000; *Boese et al.*, 2013]. The mantle earthquakes reported by *Boese et al.* [2013] directly underlie low-frequency earthquake (LFE) hypocenters [*Chamberlain et al.*, 2014] (Figures 9b and 9e) that spatially correlate with a zone of high attenuation of *P* waves (low Q_p) [*Eberhart-Phillips et al.*, 2008] and a region of high crustal electrical conductivity [*Wannamaker et al.*, 2002]. The conductive and low Q_p features have been interpreted to result from fluid migration upward from a zone of high-pressure metamorphism of the relict Eocene oceanic lithosphere [*Boese et al.*, 2013; *Chamberlain et al.*, 2014]. The dehydration of this oceanic lithosphere would presumably lead to a localized zone of increased density and more brittle rheology relative to the surrounding mantle [*Karato and Jung*, 1998], localizing subcrustal seismicity within the dehydrated zone. Our results show a high V_s zone (Figures 9a–9c and 9e) coincident with the inferred zone of brittle deformation defined by the subcrustal earthquakes [*Boese et al.*, 2013]. Anomaly PM thickens to the west of the Alpine Fault and south of Mount Cook, consistent with the location of the passive margin interpreted by *Boese et al.* [2013]. Our model is consistent with the hypothesis that the thickened edge of the remnant passive margin could be localizing brittle shear strain [*Boese et al.*, 2013] at depth in the mantle. A deep high-speed zone, offset to the west of anomaly PM and the crustal root (Figures 8 and 9), could result from underthrusting of the Australian plate [*Allis*, 1981] or a combination of convergent thickening and intracontinental subduction [*Fry et al.*, 2014; *Sutherland et al.*, 2000].

Because the MOANA array completely surrounds central South Island, both group velocity resolution (Figure 5) and phase velocity RMS uncertainty (Figure 6) are improved in this region relative to the edges of the array. Therefore, we consider our V_s model of the central South Island region to be better constrained than those of the Challenger and Campbell Plateaus.

4.3. Canterbury Basin and Bounty Trough

The spatial extent of the low-velocity anomaly AU (Figure 10a) at shallow depths (Figure 8) is consistent with the regions of Cenozoic intraplate volcanism between the Otago and Banks Peninsulas. High mantle helium values measured at the Banks and Otago Peninsulas are interpreted by *Hoke et al*. [2000] to derive from relatively recent asthenospheric melts, perhaps originating from the lithosphere-asthenosphere boundary at about 80 km depth and which coincide with measurements of high heat flow. *Hoernle et al*. [2006] propose that the Cenozoic shield volcanism beneath Otago can be explained by asthenospheric upwelling into cavities produced by lithospheric delamination, which thus do not require a plume origin. The lateral extent of anomaly AU at 60–140 km depth is consistent with the latter interpretation, but the limited vertical extent of our model (<150 km) precludes ruling out a plume-like feature (Figure 9). The stalling of Hikurangi subduction along the Chatham Rise has been proposed to result in slab detachment and subsequent asthenospheric upwelling in the last 20 Ma [*Davy et al*., 2008]. The lowest seismic shear wave speeds in anomaly AU at depths greater than 100 km in our model (Figures 8f–8h) form a region subparallel to the Chatham Rise fossil margin, as would be expected for a convective upwelling caused by slab detachment inboard of the Chatham Rise margin.

While the geometry of the MOANA array limits raypath coverage on Campbell Plateau to the SE of the South Island and confines our modeled area to a small region (e.g., Figure 8), the RMS uncertainties of teleseismic phase velocity measurements (the main control on deeper structure in our models) are low relative to those on Challenger Plateau off the west coast of the South Island (Figure 6b). Thus, we consider the mantle low-velocity structure we image here to be robustly constrained by our data.

4.4. Inferred Lithospheric Thickness Variations

Defining the base of the lithosphere using the 4.5 km/s shear wave velocity contour as a proxy allows us to gauge first-order changes in the thickness of the high-velocity lid across the MOANA array. Beneath the inner Campbell Plateau off the east coast we image the thinnest lid in our model, where the 4.5 km/s contour ranges from <75 km depth to nearly absent beneath a portion of the east coast, south of Banks Peninsula (Figure 9). The maximum lithospheric thickness of over 150 km (exceeding the depth extent of our model) occurs beneath the western coast of the South Island and could be related to the presence of subducted Pacific lithosphere (D. W. Zietlow et al., submitted to *Journal of Geophysical Research*, 2016). Lithospheric thicknesses elsewhere in our model average ~80 km beneath the Challenger Plateau and the Eastern Campbell Plateau (Figure 9).

Zietlow et al. [2014] used measurements of teleseismic shear wave splitting to distinguish between distributed and localized deformation at depth in the plate boundary. In that work the authors hypothesized that given a lithospheric thickness of ~150 km, all distributed shear resulting in the measured anisotropy could be accommodated purely in the lithosphere. The lithospheric thickness we estimate of ~140 km beneath western South Island supports this model of distributed deformation in the lithosphere.

Beneath the east coast of South Island and Inner Bounty Trough, we image substantially thinner lithosphere (<75 km) than that of Challenger Plateau beneath the west coast of the South Island (>140 km). Based on petrological analysis of Cenozoic Dunedin and Otago volcanics, *Hoke et al*. [2000] predict a lithospheric thickness of ~80 km in the region and an asthenospheric source for the magma. Our models indicate that Campbell Plateau lithosphere is indeed on the order of 80 km thick (Figure 9), consistent with a model of asthenospheric upwelling resulting from slab detachment beneath the stalled Hikurangi subduction margin at Chatham Rise [*Hoernle et al*., 2006; *Davy et al*., 2008].

5. Conclusions

Ambient seismic noise and teleseismic surface wave data recorded on continuous vertical components from 29 broadband OBS and 28 broadband land seismometers deployed in the South Island region of New Zealand have been analyzed for Rayleigh wave phase and group velocity variations at periods between 8 and 70 s. By inverting these data we have constructed the first onshore/offshore lithospheric shear velocity model extending beneath the Challenger and Campbell Plateaus adjacent to the South Island.

We observe that the lithospheric thickness beneath the western South Island is substantially greater than that of inner Campbell Plateau. Our estimate of the inner Campbell Plateau thickness is comparable to the 80 km

predicted by *Hoke et al*. [2000], given an asthenospheric origin of South Island volcanics. The thickest lithosphere we image occurs beneath the west coast of the South Island and south of Mount Cook and could result from underthrusting of Australian plate lithosphere [*Allis*, 1981] or a combination of convergent thickening and subduction [*Fry et al*., 2014; *Sutherland et al*., 2000]. The spatial extent of this thick, high-speed anomaly in our models corresponds with the presumed location of a remnant Eocene passive margin [*Boese et al*., 2013; *Sutherland et al*., 2000] that has been proposed to control present-day deformation along the Alpine Fault.

We also image a low-velocity feature beneath the Banks and Otago Peninsulas, which correlates with surface observations of mantle-sourced helium isotopes to support the existence of upwelling asthenosphere beneath this area [*Hoke et al*., 2000; *Hoernle et al*., 2006].

To the northwest of the South Island we model a high-velocity body consistent with the subduction of Pacific plate oceanic lithosphere. The boundaries of this anomaly coincide with those of inferred preexisting subduction structures [*Davey*, 2005; *Melhuish et al*., 2005]. These features all strike subparallel to both the paleo-Pacific Gondwana Margin and the present-day Alpine Fault, implying that the location and geometry of the Cenozoic Australian-Pacific plate boundary in New Zealand could be related to discontinuities inherited from the Paleozoic.

Acknowledgments

We thank the Captain and Crew of the R/V *Thomas G. Thompson* (cruise TN229) in 2009, the R/V *Roger Revelle* (cruise RR1002) in 2010, and the SIO OBSIP facility for the expert assistance at sea. The instruments used in this field program were provided by the U.S. National Ocean Bottom Seismic Instrumentation Pool (http://www.obsip.org). Seismic data are archived at the IRIS Data Management Center. We used the Generic Mapping Tools software package [*Wessel et al*., 2009] for creating all maps and cross sections shown herein. The CPS 330 software package [*Herrmann and Ammon*, 1998] was instrumental in this work. The collection of seismic data was funded by the National Science Foundation under grants EAR-0409564, EAR-0409609, and EAR-0409835. J. Stachnik was funded in part by the CIRES postdoctoral fellowship program. F.-C. Lin was supported by NSF grant CyberSEES-1442665 and the King Abdullah University of Science and Technology (KAUST) under award OCRF-2014-CRG3-2300. We are grateful to Dan Zietlow, Rupert Sutherland, Laura Wallace, Peter Molnar, Martha Savage, Tim Stern, Robert Herrmann, Michael Ritzwoller, Oleg Godin, Stuart Weir, and Bill Fry for their insight and advice. We thank JGR Associate Editor Yehuda Ben-Zion and two anonymous reviewers for their helpful reviews.

References

Allis, R. G. (1981), Continental underthrusting beneath the Southern Alps of New Zealand, *Geology*, *9*(7), 303–307.

Aster, R. C., B. Borchers, and C. H. Thurber (2013), *Parameter estimation and inverse problems*, 2nd ed., pp. 245–246, Elsevier, Amsterdam.

Bache, F., N. Mortimer, R. Sutherland, J. Collot, P. Rouillard, V. Stagpoole, and A. Nicol (2014), Seismic stratigraphic record of transition from Mesozoic subduction to continental breakup in the Zealandia sector of eastern Gondwana, *Gondwana Res.*, *26*(3–4), 1060–1078, doi:10.1016/j.gr.2013.08.012.

Ball, J. S., A. F. Sheehan, J. C. Stachnik, F.-C. Lin, and J. A. Collins (2014), A joint Monte Carlo analysis of seafloor compliance, Rayleigh wave dispersion, and receiver functions at ocean bottom seismic stations offshore New Zealand, *Geochem. Geophys. Geosyst.*, *15*, 5051–5068, doi:10.1002/2014GC005412.

Barmin, M. P., M. H. Ritzwoller, and A. L. Levshin (2001), A fast and reliable method for surface wave tomography, in *Monitoring the Comprehensive Nuclear-Test-Ban Treaty: Surface Waves*, pp. 1351–1375, Basel, Birkhäuser.

Bassin, C., G. Laske, and G. Masters (2000), The current limits of resolution for surface wave tomography in North America, *Eos Trans. AGU*, 81, F897.

Becker, J. J., et al. (2009), Global bathymetry and elevation data at 30 arc seconds resolution: SRTM30_PLUS, *Mar. Geod.*, *32*(4), 355–371, doi:10.1080/01490410903297766.

Bensen, G., M. Ritzwoller, M. Barmin, A. Levshin, F. Lin, M. Moschetti, N. Shapiro, and Y. Yang (2007), Processing seismic ambient noise data to obtain reliable broad-band surface wave dispersion measurements, *Geophys. J. Int.*, *169*, 1239–1260.

Boese, C. M., T. A. Stern, J. Townend, S. Bourguignon, A. Sheehan, and E. G. C. Smith (2013), Sub-crustal earthquakes within the Australia–Pacific plate boundary zone beneath the Southern Alps, *N. Z. Earth Planet. Sci. Lett.*, *376*, 212–219, doi:10.1016/j.epsl.2013.06.030.

Bradshaw, J. D., M. Gutjahr, S. D. Weaver, and K. N. Bassett (2009), Cambrian intra-oceanic arc accretion to the austral Gondwana Margin: Constraints on the location of proto-New Zealand, *Aust. J. Earth Sci.*, *56*(4), doi:10.1080/08120090902806339.

Cande, S. C., and J. M. Stock (2004), Pacific-Antarctic-Australia motion and the formation of the Macquarie Plate, *Geophys. J. Int.*, *157*, 399–414, doi:10.1111/j.1365-246X.2004.02224.x.

Chamberlain, C. J., D. R. Shelly, J. Townend, and T. A. Stern (2014), Low-frequency earthquakes reveal punctuated slow slip on the deep extent of the Alpine Fault, New Zealand, *Geochem. Geophys. Geosyst.*, *15*, 2984–2999, doi:10.1002/2014GC005436.

Collins, J. A., and P. H. Molnar (2014), Pn anisotropy beneath the South Island of New Zealand and implications for distributed deformation in continental lithosphere, *J. Geophys. Res. Solid Earth*, *119*, 7745–7767, doi:10.1002/2014JB011233.

Cooper, R. A., and A. J. Tulloch (1992), Early Palaeozoic terranes in New Zealand and their relationship to the Lachlan Fold Belt, *Tectonophysics*, *214*(1), 129–144, doi:10.1016/0040-1951(92)90193-A.

Crawford, W. C., and S. C. Webb (2000), Identifying and removing tilt noise from low-frequency ($<$0.1 Hz) seafloor vertical seismic data, *Bull. Seismol. Soc. Am.*, *90*, 952–963, doi:10.1785/0120070050.

Davey, F. J. (2005), A Mesozoic crustal suture on the Gondwana Margin in the New Zealand region, *Tectonics*, *24*, TC4006, doi:10.1029/2004TC001719.

Davy, B., K. Hoernle, and R. Werner (2008), Hikurangi Plateau: Crustal structure, rifted formation, and Gondwana subduction history, *Geochem. Geophys. Geosyst.*, *9*, Q07004, doi:10.1029/2007GC001855.

Dziewonski, A., and A. Hales (1972), Numerical analysis of dispersed seismic waves, *Methods Comput. Phys.*, *11*, 39–85.

Dziewonski, A. M., A. L. Hales, and E. R. Lapwood (1975), Parametrically simple Earth models consistent with geophysical data, *Phys. Earth Planet Int.*, *10*(1), 12–48, doi:10.1016/0031-9201(75)90017-5.

Eberhart-Phillips, D., M. Chadwick, and S. Bannister (2008), Three-dimensional attenuation structure of central and southern South Island, New Zealand, from local earthquakes, *J. Geophys. Res.*, *113*, B05308, doi:10.1029/2007JB005359.

Federico, L., L. Crispinia, G. Capponia, and J. D. Bradshaw (2009), The Cambrian Ross Orogeny in northern Victoria Land (Antarctica) and New Zealand: A synthesis, *Gondwana Res.*, *15*(2), 188–196, doi:10.1016/j.gr.2008.10.004.

Fry, B., D. Eberhart-Phillips, and F. Davey (2014), Mantle accommodation of lithospheric shortening as seen by combined surface wave and teleseismic imaging in the South Island, New Zealand, *Geophys. J. Int.*, *199*, 499–513, doi:10.1093/gji/ggu271.

Gaite, B., A. Villaseñor, A. Iglesias, M. Herraiz, and I. Jiménez-Munt (2015), A 3-D shear velocity model of the southern North American and Caribbean plates from ambient noise and earthquake tomography, *Solid Earth*, *6*, 271–284, doi:10.5194/se-6-271-2015.

Herrmann, R. B., and C. J. Ammon (2004), Surface waves, receiver functions and crustal structure *Computer Programs in Seismology*, *Version 3.30*, St. Louis Univ., Saint Louis, Mo.

Hoernle, K., J. D. L. White, P. van den Bogaard, F. Hauff, D. S. Coombs, R. Werner, C. Timm, D. Garbe-Schönberg, A. Reay, and A. F. Cooper (2006), Cenozoic intraplate volcanism on New Zealand: Upwelling induced by lithospheric removal, *Earth Planet. Sci. Lett.*, *248*(1-2), 350–367, doi:10.1016/j.epsl.2006.06.001.

Hoke, L., R. Poreda, A. Reay, and D. Weaver (2000), The subcontinental mantle beneath southern New Zealand, characterized by helium isotopes in intraplate basalts and gas-rich springs, *Geochim. Cosmochim. Acta*, *64*, 2489–2507.

Hosseini, S. M. (2014), Reducing uncertainties in the velocities determined by inversion of phase velocity dispersion curves using synthetic seismograms, PhD thesis, Univ. of Memphis.

Karato, S., and H. Jung (1998), Water, partial melting and the origin of the seismic low velocity and high attenuation zone in the upper mantle, *Earth Planet. Sci. Lett.*, *157*(3–4), 193–207, doi:10.1016/S0012-821X(98)00034-X.

Kennett, B. L. N., E. R. Engdahl, and R. Buland (1995), Constraints on seismic velocities in the Earth from travel times, *Geophys. J. Int.*, *122*, 108–124.

Kohler, M. D., and D. Eberhart-Phillips (2002), Three-dimensional lithospheric structure below the New Zealand Southern Alps, *J. Geophys. Res.*, *107*(B10, 2225), doi:10.1029/2001JB000182.

Kohler, M. D., and D. Eberhart-Phillips (2003), Intermediate-depth earthquakes in a region of continental convergence: South Island, New Zealand, *Bull. Seismol. Soc. Am.*, *93*(1), 85–93.

Levshin, A. L., V. F. Pisarenko, and G. A. Pogrebinsky (1972), On a frequency-time analysis of oscillations, *Ann. Geophys.*, *28*, 211–218.

Lin, F., M. H. Ritzwoller, J. Townend, M. Savage, and S. Bannister (2007), Ambient noise Rayleigh wave tomography of New Zealand, *Geophys. J. Int.*, doi:10.1111/j.1365-246X.2007.03414.x.

Lin, F.-C., M. H. Ritzwoller, and R. Snieder (2009), Eikonal Tomography: Surface wave tomography by phase-front tracking across a regional broad-band seismic array, *Geophys. J. Int.*, *177*, 1091–1110, doi:10.1111/j.1365-246X.2009.04105.x.

Lin, F. C., and M. H. Ritzwoller (2011), Helmholtz surface wave tomography for isotropic and azimuthally anisotropic structure, *Geophys. J. Int.*, *186*, doi:10.1111/j.1365-246X.2011.05070.x.

Lin, F. C., D. Li, R. W. Clayton, and D. Hollis (2013), High-resolution 3-D shallow crustal structure in Long Beach, California: Application of ambient noise tomography on a dense seismic array, *Geophysics*, *78*(4), Q45–Q56, doi:10.1190/geo2012-0453.1.

Lin, F.-C., M. P. Moschetti, and M. H. Ritzwoller (2008), Surface wave tomography of the western United States from ambient seismic noise: Rayleigh and Love wave phase velocity maps, *Geophys. J. Int.*, *173*, 281–298, doi:10.1111/j.1365-246X.2008.03720.x.

Melhuish, A., W. S. Holbrook, F. Davey, D. A. Okaya, and T. Stern (2005), Crustal and upper mantle seismic structure of the Australian Plate, South Island, New Zealand, *Tectonophysics*, *395*(1–2), 113–135, doi:10.1016/j.tecto.2004.09.005.

Nafe, J. E., and C. L. Drake (1957), Variation with depth in shallow and deep water marine sediments of porosity, density and the velocities of compressional and shear waves, *Geophysics*, *22*(3), 523–552.

Petersen, T., K. Gledhill, M. Chadwick, N. H. Gale, and J. Ristau (2011), The New Zealand National Seismograph Network, *Seismol. Res. Lett.*, *82*(1), 9–20, doi:10.1785/gssrl.82.1.9.

Pysklywec, R. N., S. M. Ellis, and A. R. Gorman (2010), Three-dimensional mantle lithosphere deformation at collisional plate boundaries: A subduction scissor across the South Island of New Zealand, *Earth Planet. Sci. Lett.*, *289*, 334–346, doi:10.1016/j.epsl.2009.11.022.

Reyners, M. (2013), The central role of the Hikurangi Plateau in the Cenozoic tectonics of New Zealand and the Southwest Pacific, *Earth Planet. Sci. Lett.*, *361*, 460–468, doi:10.1016/j.epsl.2012.11.010.

Salmon, M., B. L. N. Kennett, T. Stern, and A. R. A. Aitken (2013), The Moho in Australia and New Zealand, *Tectonophysics*, *609*, 288–298, doi:10.1016/j.tecto.2012.07.009.

Smith, W. H. F., and P. Wessel (1990), Gridding with continuous curvature splines in tension, *Geophysics*, *55*, 293–305.

Spasojević, S., and R. W. Clayton (2008), Crustal structure and apparent tectonic underplating from receiver function analysis in South Island, New Zealand, *J. Geophys. Res.*, *113*, B04307, doi:10.1029/2007JB005166.

Stachnik, J., K. Dueker, D. Schutt, and H. Yuan (2008), Imaging Yellowstone plume-lithosphere interactions from inversion of ballistic and diffusive Rayleigh wave dispersion and crustal thickness data, *Geochem. Geophys. Geosyst.*, *9* Q06,004, doi:10.1029/2008GC001992.

Sutherland, R. (1999), Basement geology and tectonic development of the greater New Zealand region, *Tectonophysics*, *308*(3), 341–362, doi:10.1016/S0040-1951(99)00108-0.

Sutherland, R., F. Davey, and J. Beavan (2000), Plate boundary deformation in South Island, New Zealand, is related to inherited lithospheric structure, *Earth Planet. Sci. Lett.*, *177*, 141–151, doi:10.1016/S0012-821X(00)00043-1.

Wannamaker, P. E., G. R. Jiracek, J. A. Stodt, T. G. Caldwell, V. M. Gonzalez, J. D. McKnight, and A. D. Porter (2002), Fluid generation and pathways beneath an active compression orogen, the New Zealand Southern Alps, inferred from magnetotelluric data, *J. Geophys. Res.*, *107*(B6), 2117, doi:10.1029/2001JB000186.

Webb, S. C., and W. C. Crawford (1999), Long period seafloor seismology and deformation under ocean waves, *Bull. Seismol. Soc. Am.*, *89*(6), 1535–1542.

Wessel, P., W. H. F. Smith, R. Scharroo, J. F. Luis, and F. Wobbe (2013), Generic Mapping Tools: Improved version released, *Eos Trans. AGU*, *94*, 409–410, doi:10.1002/2013EO450001.

Yang, Z., A. F. Sheehan, J. A. Collins, and G. Laske (2012), The character of seafloor ambient noise recorded offshore New Zealand: Results from the MOANA ocean bottom seismic experiment, *Geochem. Geophys. Geosyst.*, *13*, Q10011, doi:10.1029/2012GC004201.

Yao, H., and R. D. van der Hilst (2009), Analysis of ambient noise energy distribution and phase velocity bias in ambient noise tomography, with applications to SE Tibet, *Geophys. J. Int.*, *179*, 1113–1132, doi:10.1111/j.1365-246X.2009.04329.x.

Yao, H., P. Gouedard, J. A. Collins, J. J. McGuire, and R. D. van der Hilst (2011), Structure of young East Pacific Rise lithosphere from ambient noise correlation analysis of fundamental- and higher-mode Scholte-Rayleigh waves, *C. R. Geosci.*, *343*(8), 571–583.

Yeck, W. L. (2015), Investigation into the deformation of the lithosphere past and present using passive seismic methods: Case studies of the Wyoming Craton and South Island of New Zealand, PhD thesis, 158 pp., Univ. of Colorado at Boulder.

Zietlow, D. W., A. F. Sheehan, P. H. Molnar, M. K. Savage, G. Hirth, J. A. Collins, and B. H. Hager (2014), Upper mantle seismic anisotropy at a strike-slip boundary: South Island, New Zealand, *J. Geophys. Res. Solid Earth*, *119*, 1020–1040, doi:10.1002/2013JB010676.